International Journal of Solids and Structures 47 (2010) 947–956

Contents lists available at ScienceDirect

International Journal of Solids and Structures

journal homepage: www.elsevier.com/locate/ijsolstr

A method of analysis for end and transitional effects in anisotropic cylinders

C. Alpdogan [a], S.B. Dong [b], E. Taciroglu [b,*]

[a] MMI Engineering Inc., Oakland, CA 94612, USA
[b] Department of Civil and Environmental Engineering, University of California, Los Angeles, CA 90095, USA

ARTICLE INFO

Article history:
Received 18 August 2009
Received in revised form 24 November 2009
Available online 22 December 2009

Keywords:
Saint–Venant solutions
Saint–Venant's principle
End effects
Transition effects
Delamination
Composites

ABSTRACT

We present a rigorous verification study and an extension to an existing semi-analytical finite element formulation for analysis of end and transition effects in prismatic cylinders. End and transition effects in stressed cylinders are phenomena associated with the difference between results that are predicted by the Saint–Venant solutions and the actual point-wise conditions. These differences manifest themselves as self-equilibrated stress states. Notwithstanding certain well-known exceptions (e.g., restrained torsion of open thin-walled sections), such effects in isotropic cylinders are usually confined to a very small neighborhood of a terminal boundary or transition zone, and are typically neglected. For anisotropy, as in the case of most smart/active and composite material systems, they can persist much further into the interior of the structure, and need to be quantified to design geometry transition zones and to fully understand the delamination effects. In the semi-analytical approach, we first discretize the governing equations within the cross-sectional plane of the cylinder. The end-solution fields satisfy the homogeneous form of the resulting semi-analytical system of ordinary differential equations. This leads to an algebraic eigenvalue problem, and an eigenfunction expansion of the stress and displacement fields due to end effects. Unique to the present study, we formulate a procedure to quantify the transitional effects for end-to-end connected cylinders for which the displacement and stress continuity along the transition interface need to be enforced. The semi-analytical approach has several distinct advantages: (i) It is computationally efficient, as only the cross-sectional geometry is discretized; (ii) it can be applied to arbitrary cross-sectional geometries and the most general form of anisotropy; and (iii) it yields direct measures for the decay lengths (or decay rates) of any end-or transition-solution field. Analytical solutions to end-effect problems are scarce. Those that exist are for simple geometry and material constitution. We use these analytical solutions, as well as solutions obtained using three-dimensional finite element models, to verify our approach and to assess its efficiency.

1. Introduction

When two (or possibly more) beams are joined at an interface where forces and moments are transmitted, transitional effects occur. These effects are confined to the neighborhood of the interface. With distance away from this region, the stress states return to distributions given by Saint–Venant (SV) extension, bending, torsion and flexure solutions. But in the vicinity of the interface, the behavior is highly complex and not according to aforementioned SV solutions. As illustrated in Fig. 1, a part of the behavior is self-equilibrated, representing the difference between SV data and actual end condition. This part decays with distance from an end, i.e., Saint–Venant's principle.

Herein, we are occupied with quantifying such effects in prismatic beams, whose cross-sections may be anisotropic as well as inhomogeneous. To accommodate prismatic beams with arbitrary cross-sectional geometries and general material properties, a semi-analytical finite element (SAFE) method is adopted wherein the cross-section undergoes discretization. The kinematic behavior is represented by polynomial interpolations in the elements comprising the cross-sectional model with the axial dependence left undetermined at the outset. The governing equations are of the form

$$\mathbf{K_1}\mathbf{U}_{,zz} + \mathbf{K_2}\mathbf{U}_{,z} - \mathbf{K_3}\mathbf{U} = \mathbf{0} \tag{1}$$

where the array $\mathbf{U} = \mathbf{U}(z)$ contains the nodal displacements and $\mathbf{K_1}$, $\mathbf{K_2}$, and $\mathbf{K_3}$ are system stiffness matrices. Formulation of these matrices for numerical results herein can be found in Taweel et al. (2000). The complete solution to Eq. (1) consists of three parts, i.e.,

$$\mathbf{U}(z) = \mathbf{U_{SV}} + \mathbf{U_{end}} + \mathbf{U_{rb}} \tag{2}$$

where $\mathbf{U_{SV}}$ denotes a Saint–Venant solution for a stress state corresponding to applied end forces and moments, $\mathbf{U_{end}}$ concerns self-equilibrated effects that quantifies how Saint–Venant's principle

* Corresponding author. Tel.: +1 310 2674655; fax: +1 310 206 2222.
E-mail address: etacir@ucla.edu (E. Taciroglu).

0020-7683/$ - see front matter © 2009 Elsevier Ltd. All rights reserved.
doi:10.1016/j.ijsolstr.2009.12.009

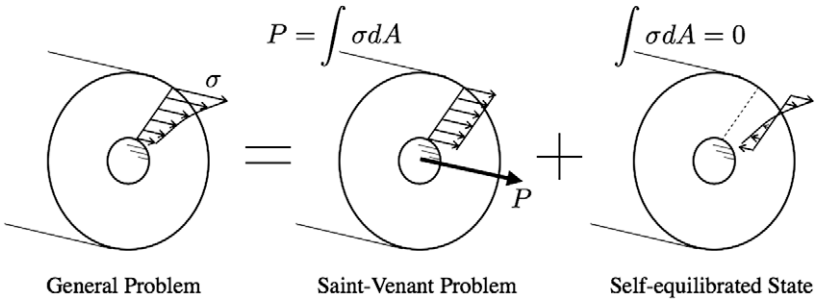

Fig. 1. Saint–Venant and self-equilibrated parts of a stress field near the ends.

works, and $\mathbf{U_{rb}}$ contains the components of rigid body motion needed to meet the prescribed kinematic constraints.

For the Saint–Venant solution, we follow the method by Dong et al. (2001) and Kosmatka et al. (2001). But we note that others have similar or alternative solution methods for this problem, viz., Giavotto et al. (1983), Ladevéze and Simmonds (1998), Popescu and Hodges (2000), El Fatmi and Zenzri (2002), El Fatmi (2007a,b), Herrmann (1965), Mason and Herrmann (1968).

To determine the end solution, take $\mathbf{U_{end}}(z) = \mathbf{U_o}e^{-\gamma z}$, where γ denotes an inverse decay length and $\mathbf{U_o}$ is a displacement vector of the self-equilibrated effects. Substitution of this solution form into Eq. (1) yields a quadratic algebraic eigenproblem given as,

$$\mathbf{K_3U_o} - \gamma\mathbf{K_2U_o} - \gamma^2\mathbf{K_1U_o} = \mathbf{0} \tag{3}$$

where γ is eigenvalue parameter. This eigenproblem can be reduced to first-order form, from which it is possible to see that both real and complex eigendata are admissible – representing the possibility of both exponential and sinusoidal decays. Numerical data by this approach have been reported by Huang and Dong (1984), Dong and Huang (1985), Goetschel and Hu (1985), Kazic and Dong (1990) and Lin et al. (2001), for a variety of problems related to orthotropic and anisotropic strips and circular cylinders as well as for general cross-sections. Inverse decay lengths have also been determined analytically from a transcendental equation of a boundary-value problem – see, Johnson and Little (1965) and Little and Childs (1967) for data on isotropic semi-infinite strips and circular cylinders, respectively. Mathematical insight enabling the quantification of Saint–Venant's principle was due to Toupin (1965) and Knowles (1966), whose strain energy inequality theorems bounded the decay from an end to exponential form. It is of interest to note, however, that Synge (1945) outlined the essence of the end solution; however, he did not offer any solutions. For a very comprehensive review of the literature on this topic, see Horgan and Knowles (1983) and Horgan (1989).

The purpose herein is to apply inverse decay data, extracted from Eq. (3), to treat end effects and transitional states for various arrangements where two beams are joined. In the next sections, details of the Saint–Venant solution and algebraic eigenproblem are reviewed. Then, results for isotropic strip and circular cylinder based on Eq. (3) are compared with Johnson and Little (1965) and Little and Childs (1967) to instill some confidence to the present numerical approach to study end and transitional effects. The steps in the analysis of end and transitional effects are set forth. Examples are then given on interlaminar stresses at the end of a laminated beam, stress transmission in a beam with a hollow cross-section reinforced by a plate, a beam with two angleply layers loaded over a portion of the end cross-section, and decaying stresses in the vicinity of two distinct beams connected end-to-end. Only loads applied at the end(s) are considered in our examples. Loading on the lateral surface of a beam – which belongs to Almansi–Michell class of problems – involves the nonhomogeneous form of Eq. (1); and the treatment of this problem may be found in Lin and Dong (2006). We will not consider this type of loading, but hasten to add that the analysis procedure described herein remains valid except for the inclusion of a particular solution.

2. Synopsis of Saint–Venant solutions

Saint–Venant's problem consists of determining the three-dimensional stress and displacement fields in a prismatic beam due to prescribed tractions at one end with full kinematic restraints on the other. What are known as Saint–Venant solutions (1855, 1856) are displacement and stress fields, which agree only in terms of the end resultants, i.e., (1) axial force (extension), (2) pure bending moments, (3) torque, and (4) flexural forces. The point-wise fields may not agree with the prescriptions at the two ends, but Saint–Venant's principle assures the validity of these solutions in the interior, i.e., away from the two ends of the beam.

In the method for Saint–Venant's solutions by Dong et al. (2001), a sequential integration procedure due to Ieşan (1986) was used to define the kinematic fields. Beginning with rigid body displacements, the first integral gave stress and strain fields uniform in z, or that appropriate for Saint–Venant extension–bending–torsion. The next integral gives fields that are at most linear in z, i.e., Saint–Venant flexure. In a Saint–Venant solution, three parts are involved in each kinematic field: (1) primal field, (2) cross-sectional warpage, and (3) rigid body motion. All of these components are functions of unknown displacement coefficients.

The displacement field $\mathbf{U_{SV}}$ for extension, bending, torsion and flexure has the form

$$\mathbf{U_{SV}}(z) = \left[\underset{(3M\times4)}{\mathbf{\Phi_{sv2}}}(z) + \underset{(3M\times4)}{\mathbf{\Psi_{sv2}}} + z\,\underset{(3M\times4)}{\mathbf{\Psi_{sv1}}}\right]\underset{(4\times1)}{\mathbf{a_{II}}} + \left[\underset{(3M\times4)}{\mathbf{\Phi_{sv1}}}(z) + \underset{(3M\times4)}{\mathbf{\Psi_{sv1}}}\right]\underset{(4\times1)}{\mathbf{a_I}} + \underset{(3M\times6)}{\mathbf{\Phi_{RB6}}} \times \underset{(6\times1)}{\mathbf{a_{RB}}} \tag{4}$$

where $(\mathbf{\Phi_{sv1}}, \mathbf{\Phi_{sv2}})$, $(\mathbf{\Psi_{sv1}}, \mathbf{\Psi_{sv2}})$, and $\mathbf{\Phi_{RB6}}$ are the primal fields and warpages for extension–bending–torsion ($sv1$) and flexure ($sv2$) problems, and the six rigid-body modes, respectively, with amplitude coefficients $\mathbf{a_I}$, $\mathbf{a_{II}}$, and $\mathbf{a_{RB}}$ given by

$$\mathbf{a_I} = [a_{I3}, a_{I4}, a_{I5}, a_{I6}]^T, \quad \mathbf{a_{II}} = [a_{II3}, a_{II4}, a_{II5}, a_{II6}]^T, \quad \text{and} \quad \mathbf{a_{RB}} = [a_{RB1}, a_{RB2}, \ldots a_{RB6}]^T. \tag{5}$$

Warpages $\mathbf{\Psi_{sv1}}$ and $\mathbf{\Psi_{sv2}}$ are independent of z. Details on their construction are given in Dong et al. (2001). Once these matrices are established, the Saint–Venant field is completely defined except for the unknown amplitudes $\mathbf{a_I}$, $\mathbf{a_{II}}$ and $\mathbf{a_{RB}}$.

Stresses in an element are given by

$$\boldsymbol{\sigma} = \mathbf{C}[z\{\mathbf{h} + \mathbf{b_1}\mathbf{\Psi_{sv1}}_i\} + \{\mathbf{b_2}\mathbf{\Psi_{sv1}}_i + \mathbf{b_1}\mathbf{\Psi_{sv2}}_i\}]\mathbf{a_{II}} + \mathbf{C}\{\mathbf{h} + \mathbf{b_1}\mathbf{\Psi_{sv1}}_i\}\mathbf{a_I}, \tag{6}$$

where $\mathbf{b_1}$ and $\mathbf{b_2}$ are the linear differential operators that perform the strain–displacement transformations; $\mathbf{C}$ is the linear elastic material stiffness matrix (c.f., Dong et al., 2001), and $\mathbf{h}$ is

$$\mathbf{h} = \begin{bmatrix} 0 & 0 & 0 & 0 \\ 0 & 0 & 0 & 0 \\ 1 & y & x & 0 \\ 0 & 0 & 0 & x \\ 0 & 0 & 0 & -y \\ 0 & 0 & 0 & 0 \end{bmatrix}. \tag{7}$$

Integrating the stresses over the cross-section Π yields the force and moment resultants.

$$\begin{aligned} &\int_\Pi \sigma_{zz}\,dx\,dy = P_z(z); \quad \int_\Pi \sigma_{zz} y\,dx\,dy = M_x(z) \\ &\int_\Pi (\sigma_{zy}x - \sigma_{zx}y)\,dx\,dy = M_z(z); \quad \int_\Pi \sigma_{zz} x\,dx\,dy = -M_y(z). \end{aligned} \tag{8}$$

These resultants can be recast in compact form using $\mathbf{h}$ of Eq. (7) as

$$\int_\Pi \mathbf{h}^T \boldsymbol{\sigma}\,dx\,dy = \mathbf{F}(z), \tag{9}$$

where $\mathbf{F}(z)$ for all six force and moment resultants at an end is given by

$$\mathbf{F}(z) = \begin{Bmatrix} P_z(z) \\ M_x(z) \\ -M_y(z) \\ M_z(z) \end{Bmatrix} = \begin{Bmatrix} P_z \\ M_x \\ -M_y \\ M_z \end{Bmatrix} + z \begin{Bmatrix} 0 \\ P_y \\ -P_x \\ 0 \end{Bmatrix} \quad \text{or} \quad \mathbf{F}(z) = \mathbf{F_0} + z\mathbf{F_1}. \tag{10}$$

In this expression, P_x and P_y are transverse shear resultants defined by

$$P_x = \int_\Pi \sigma_{xz}\,dx\,dy, \quad \text{and} \quad P_y = \int_\Pi \sigma_{yz}\,dx\,dy. \tag{11}$$

Substituting Eqs. (6) and (7) into Eq. (8) and integrating over a generic cross-section give

$$[z\boldsymbol{\kappa}_I + \boldsymbol{\kappa}_{II}]\mathbf{a_{II}} + \boldsymbol{\kappa}_I \mathbf{a_I} = \mathbf{F_0} + z\mathbf{F_1}, \tag{12}$$

where

$$\underset{(4\times4)}{\boldsymbol{\kappa}_I} = \int\int \mathbf{h}^T \boldsymbol{\sigma}_0\,dx\,dy = \begin{bmatrix} \kappa_{I33} & \kappa_{I34} & \kappa_{I35} & \kappa_{I36} \\ \kappa_{I34} & \kappa_{I44} & \kappa_{I45} & \kappa_{I46} \\ \kappa_{I35} & \kappa_{I45} & \kappa_{I55} & \kappa_{I56} \\ \kappa_{I36} & \kappa_{I46} & \kappa_{I56} & \kappa_{I66} \end{bmatrix}, \tag{13}$$

$$\underset{(4\times4)}{\boldsymbol{\kappa}_{II}} = \int\int \mathbf{h}^T \boldsymbol{\sigma}_1\,dx\,dy = \begin{bmatrix} \kappa_{II33} & \kappa_{II34} & \kappa_{II35} & \kappa_{II36} \\ \kappa_{II34} & \kappa_{II44} & \kappa_{II45} & \kappa_{II46} \\ \kappa_{II35} & \kappa_{II45} & \kappa_{II55} & \kappa_{II56} \\ \kappa_{II36} & \kappa_{II46} & \kappa_{II56} & \kappa_{II66} \end{bmatrix}. \tag{14}$$

Differentiating equation (12) yields the governing equations for the flexure forces, P_y and P_x. To wit,

$$\boldsymbol{\kappa}_I \mathbf{a_{II}} = \mathbf{F_1}. \tag{15}$$

Once $\mathbf{a_{II}}$ is determined, Eq. (12) may be re-applied with $z = 0$ to give the solution for $\mathbf{a_I}$ in terms of the axial force, bending moments and torque (P_z, M_x, M_y, M_z) at the end of the beam, as in

$$\boldsymbol{\kappa}_I \mathbf{a_I} = \mathbf{F_0} - \boldsymbol{\kappa}_{II} \mathbf{a_{II}}. \tag{16}$$

Lastly, the coefficients $\mathbf{a_{RB6}}$ of the rigid body displacements can be determined from the restraint conditions at the other end (i.e., at $z = L$) of the beam.

3. Self-equilibrated solutions

Self-equilibrated effects are represented by the solution $\mathbf{U_{end}}$ to Eq. (3). Using an exponential solution form for it – i.e., $\mathbf{U_{end}}(z) = \mathbf{U_o} e^{\gamma z}$ – and reducing Eq. (3) to first-order form yield

$$\begin{bmatrix} \mathbf{0} & \mathbf{K_3} \\ \mathbf{K_3} & \mathbf{K_2} \end{bmatrix} \begin{Bmatrix} \mathbf{U_0} \\ \mathbf{U_1} \end{Bmatrix} = \gamma \begin{bmatrix} \mathbf{K_3} & \mathbf{0} \\ \mathbf{0} & \mathbf{K_1} \end{bmatrix} \begin{Bmatrix} \mathbf{U_0} \\ \mathbf{U_1} \end{Bmatrix} \quad \text{or} \quad \mathbf{AQ_r} = \gamma \mathbf{BQ_r}, \tag{17}$$

where $\mathbf{U_1} = \gamma \mathbf{U_0}$. The combined column $\mathbf{Q_r}$ represents a right-handed system of generalized coordinates. Note that $\mathbf{K_1}$ and $\mathbf{K_3}$ are symmetric, while $\mathbf{K_2}$ is antisymmetric. Hence, the algebraic eigensystem in Eq. (17) contains both real and complex conjugate pairs of eigendata and well as zero values. Zero values indicate no decay with distance along z and these modes are the Saint–Venant solutions of extension, bending, torsion and flexure. Non-zero roots represent attenuation rates of self-equilibrated effects into the interior of the cylinder. The real and complex roots correspond to monotonic and sinusoidal decays, respectively. Positive real roots and complex roots with positive real parts represent decay into the region $z \geqslant 0$, which applies to tip-end conditions. The other subset of negative real roots and complex roots with negative real parts are for root-end conditions. The eigenvalue with the smallest magnitude real part is prominent; it defines the inverse decay length with the furthest penetration into the interior.

The eigensolution to Eq. (17) may be stated as a transformation to a right-handed system of normal coordinates $\mathbf{X}$ as

$$\mathbf{Q}_r = \boldsymbol{\Phi}\mathbf{X}, \tag{18}$$

where $\boldsymbol{\Phi}$ is the right modal matrix, which can be partitioned into upper and lower parts leading to

$$\mathbf{Q_r} = \begin{bmatrix} \mathbf{U_0} \\ \mathbf{U_1} \end{bmatrix} = \begin{bmatrix} \boldsymbol{\Phi_u} \\ \boldsymbol{\Phi_l} \end{bmatrix} \mathbf{X} = \begin{bmatrix} \boldsymbol{\Phi_u} \\ \boldsymbol{\Phi_u \Gamma} \end{bmatrix} \mathbf{X}, \tag{19}$$

where $\boldsymbol{\Gamma}$ is a diagonal matrix of eigenvalues. Stress eigenvectors may be computed using the upper half of the displacement eigenvectors $\boldsymbol{\Phi_u}$ and Eq. (6).

Associated with Eq. (17) is the adjoint problem given by

$$\begin{bmatrix} \mathbf{0} & \mathbf{K_3} \\ \mathbf{K_3} & -\mathbf{K_2} \end{bmatrix} \begin{Bmatrix} \mathbf{V_0} \\ \mathbf{V_1} \end{Bmatrix} = \gamma \begin{bmatrix} \mathbf{K_3} & \mathbf{0} \\ \mathbf{0} & \mathbf{K_1} \end{bmatrix} \begin{Bmatrix} \mathbf{V_0} \\ \mathbf{V_1} \end{Bmatrix} \quad \text{or} \quad \mathbf{AQ_l} = \gamma \mathbf{BQ_l}, \tag{20}$$

where $\mathbf{Q_l}$ are left-handed generalized coordinates. The eigensolution to Eq. (20) yields the same eigenvalues as Eq. (17), but the modal matrix $\boldsymbol{\Psi}$ contain left-handed eigenvectors.

The right and left-handed eigenvectors satisfy the bi-orthogonality relations

$$\begin{aligned} &\boldsymbol{\Psi}^T \mathbf{B} \boldsymbol{\Phi} \equiv diag(B_1, B_2, \ldots, B_N) \equiv \boldsymbol{\beta} \\ &\boldsymbol{\Psi}^T \mathbf{A} \boldsymbol{\Phi} \equiv diag(\gamma_1 B_1, \gamma_2 B_2, \ldots, \gamma_N B_N), \end{aligned} \tag{21}$$

which may be stated in terms of the upper forms as

$$\begin{aligned} &\boldsymbol{\Psi}_\mathbf{u}^T \mathbf{K_3} \boldsymbol{\Phi_u} + \gamma_m \gamma_n \boldsymbol{\Psi}_\mathbf{u}^T \mathbf{K_1} \boldsymbol{\Phi_u} = \delta_{mn} B_n \\ &(\gamma_m + \gamma_n) \boldsymbol{\Psi}_\mathbf{u}^T \mathbf{K_3} \boldsymbol{\Phi_u} + \gamma_m \gamma_n \boldsymbol{\Psi}_\mathbf{u}^T \mathbf{K_2} \boldsymbol{\Phi_u} = \delta_{mn} \gamma_n B_n, \end{aligned} \tag{22}$$

where δ_{ij} is the Kronecker delta. These bi-orthogonality relations enable expansion of any arbitrary vector $\mathbf{F}$ in terms of the right-handed eigenvectors. This expansion has the form

$$\mathbf{F} = \boldsymbol{\Phi}_u \boldsymbol{\alpha} \tag{23}$$

with $\boldsymbol{\alpha}$ denoting an array of amplitudes. Applying bi-orthogonality relations, Eq. (23) yields the amplitudes as

$$\boldsymbol{\alpha} = \boldsymbol{\beta}(\boldsymbol{\Psi}_\mathbf{u}^T \mathbf{K_3} + \gamma_n^2 \boldsymbol{\Psi}_u^T \mathbf{K_1}) \mathbf{F}. \tag{24}$$

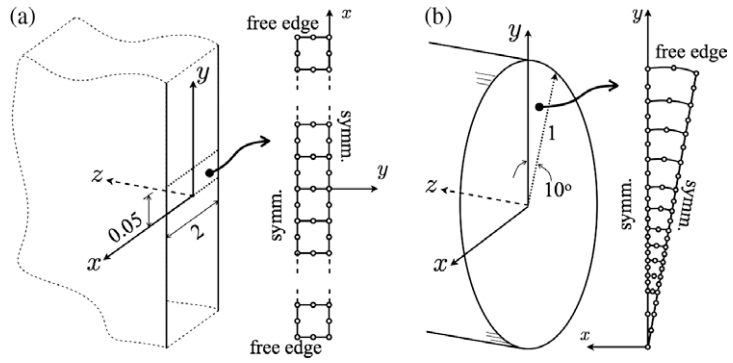

Fig. 2. Geometry and the finite element models of (a) the semi-infinite elastic strip and (b) the circular wedge.

Table 1
Comparison of the semi–infinite elastic strip data.

	Present method		Johnson and Little (1965)	
Modes	Re$\lvert\alpha_n\rvert$	Im$\lvert\alpha_n\rvert$	Re$\lvert\gamma_n\rvert$	Im$\lvert\gamma_n\rvert$
1–4	±3.74884	±i1.38435	1.38434	±i3.74884
5–8	±6.95013	±i1.67603	1.67611	±i6.94998
9–12	±10.12033	±i1.85742	1.85838	±i10.11926
13–16	±13.28161	±i1.98637	1.99157	±i13.27727
17–20	±16.44313	±i2.07731	2.09663	±i16.42987
21–24	±19.61327	±i2.12607	2.18340	±i19.57941
25–28	±22.80485	±i2.10934	2.25732	±i22.72704
29–32	±26.04899	±i1.96465	2.32171	±i25.87339
33–36	±29.36078	±i2.45709	2.37876	±i29.01883
37–40	±32.56340	±i2.87380	2.42996	±i32.16362

4. Verification problems: the semi-infinite strip and circular cylinder

In order to verify such eigendata extracted with our computer code, we compared results with those obtained analytically by Johnson and Little (1965) and Little and Childs (1967) for a semi-infinite rectangular strip and a solid circular cylinder, respectively. The geometry and the finite element models of these two problems are schematically shown in Fig. 2. For semi-infinite strip, a 0.05×2 region was meshed with 40 quadrilateral finite elements and appropriate symmetry boundary conditions were applied. For the semi-infinite circular cylinder, a 10-degree wedge was meshed with 35 quadrilateral finite elements (only a coarser mesh is shown in figure). Displacements were constrained in the direction normal to the wedge boundaries.

A subset of the fundamental eigenvalues by the present (SAFE) method is presented in Table 1 along with analytical data of Johnson and Little (1965); and there is a very good agreement between the two sets of results. The transposition of real and imaginary parts in the two sets of data is due to different definitions of the eigenvalues. We also note that the SAFE method yields both positive and negative real parts of the eigenvalues for decay in both axial directions, where the analytical results were quoted in Johnson and Little (1965) for decay in one direction only. That the agreement is better for the lowest modes – with larger deviations observed in the ascending modes – is consistent with finite element modeling realities for data involving higher spatial variations.

For the circular cylinder, the analytical solution by Little and Childs (1967) provides only axisymmetric data, which are compared with the SAFE method's results in Table 2 for two different values of the Poisson's ratio. As seen in this table, the agreement is also very good, and the patterns by which the accuracy diminishes with higher modes is the same as seen in the rectangular strip problem.

Table 2
Subsets of eigenvalues.

Mode	Present method	Little and Childs (1967)
Case 1 ($E = 1.0, \nu = 0.0$)		
1–4	±2.55678 ± i1.38897	2.55677 ± i1.38897
5–8	±6.00607 ± i1.63864	6.00586 ± i1.63870
9–12	±9.23447 ± i1.82863	9.23317 ± i1.82906
13–16	±12.42245 ± i1.96625	12.41789 ± i1.96788
17–20	±15.59555 ± i2.06945	15.58596 ± i2.07680
21–24	±18.76768 ± i2.12565	18.74560 ± i2.16636
25–28	±22.00042 ± i2.12493	21.90036 ± i2.24238
29–32	±25.30433 ± i2.16664	25.05201 ± i2.30840
Case 2 ($E = 1.0, \nu = 0.3$)		
1–4	±2.77219 ± i1.36219	2.72218 ± i1.36210
5–8	±6.06039 ± i1.63733	6.06008 ± i1.63762
9–12	±9.26858 ± i1.82621	9.26684 ± i1.82826
13–16	±12.44788 ± i1.95882	12.44253 ± i1.96724
17–20	±15.61297 ± i2.04381	15.60544 ± i2.07628
21–24	±18.78131 ± i2.02946	18.76174 ± i2.16593
25–28	±22.07817 ± i1.85840	21.91414 ± i2.24202
29–32	±25.54335 ± i1.62361	25.06403 ± i2.30810

Using the axisymmetric data, we also considered the decay of a self-equilibrated stress state given by $\sigma_{zz} = 1 - 2r^2$ and $\sigma_{rz} = 2.4r - 2.6r^3 + 0.2r^5$ in the radial (r) direction. Without any loss of generality, Poisson's ratio was set at $\nu = 0.3$. It is self-evident that the radial shear stress distribution leads to no resultant force. Integration of the axial stress distribution of the cross-section also shows a null resultant axial force, i.e.,

$$\int_{\Pi} \sigma_{zz} r \, dr \, d\theta \equiv 0. \tag{25}$$

Using the Saint–Venant solution data and the stress eigenvectors, plots of four stress components in the radial direction at various distances along the axis of the cylinder are shown in Fig. 3. The quantitative manner in which the decay occurs can be seen. We note that the SAFE results are in very good agreement with those predicted analytically by Little and Childs (1967).

5. Analysis of end and transitional effects

5.1. End effects in a beam

Prior to getting into a discussion on transitional effects when there is a discontinuity in cross-sectional geometry, or material constitution, or both, we review the analysis of end effects in a cantilevered beam below. This analysis was set forth by Lin et al. (2001).

The displacement and corresponding stress fields may be written as

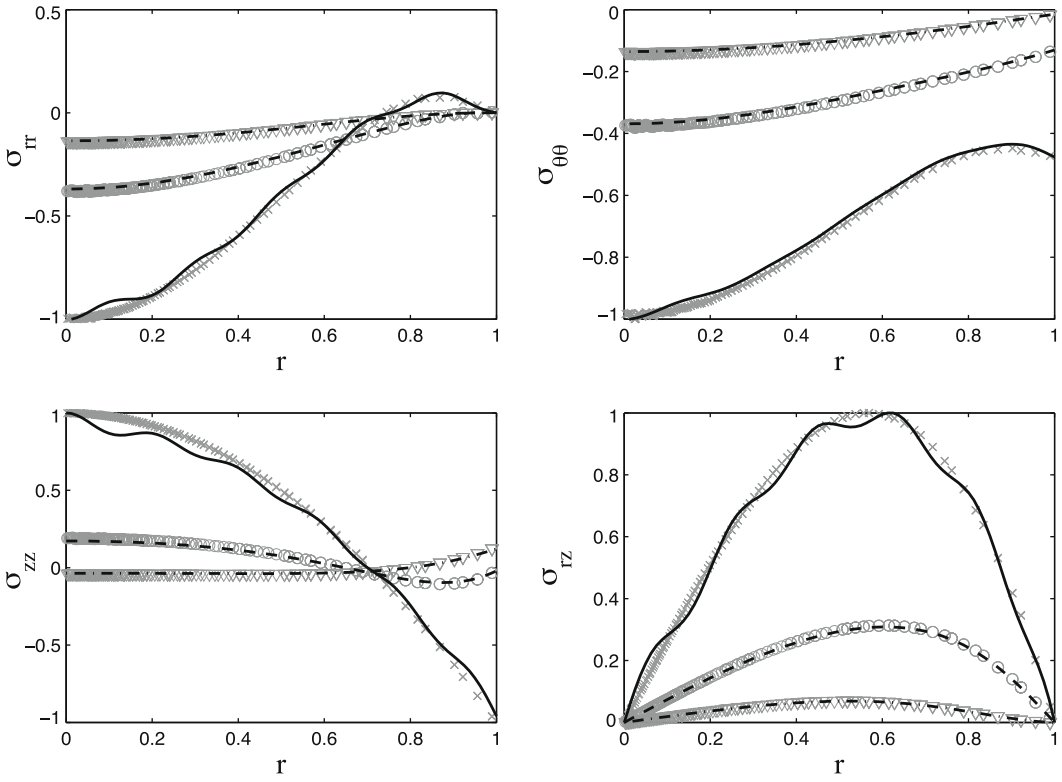

Fig. 3. Validation for stress boundary problem of a solid cylinder: The results are the distributions of non-zero stress components ($\sigma_{rr}, \sigma_{\theta\theta}, \sigma_{zz}$ and σ_{rz}) over the thickness at different cross-sections ($z/r = 0(\triangledown); 0.3(\bigcirc); 0.6(\times)$). The symbols and the (dashed, dotted, etc.) lines denote the present solutions and the analytical solutions provided by (Little and Childs, 1967), respectively.

$$\begin{aligned}\mathbf{U}(z) &= \mathbf{U}_{\mathrm{SV}}(z) + \mathbf{\Phi}_{\mathbf{RB6}}(z)\mathbf{a}_{\mathbf{RB}} + \mathbf{U}_{end}(z)\\ &= \mathbf{U}_{\mathrm{SV}}(z) + \mathbf{\Phi}_{\mathbf{RB6}}(z)\mathbf{a}_{\mathbf{RB}} + \mathbf{\Phi} diag(\mathbf{e}^{-\gamma_i z})\mathbf{a},\\ \mathbf{S}(z) &= \mathbf{S}_{\mathrm{SV}}(z) + \mathbf{S}_{end}(z) = \mathbf{S}_{\mathrm{SV}}(z) + \mathbf{S}_{end} diag(\mathbf{e}^{-\gamma_i z})\mathbf{a},\end{aligned} \tag{26}$$

where $diag(\mathbf{e}^{-\gamma_i z})$ is a diagonal matrix of exponential decays and $\mathbf{a}$ contains the undetermined amplitudes of the decaying modes. Notation $\mathbf{S}$ denotes stress components, $(\sigma_{zz}, \sigma_{yz}, \sigma_{xz})$, evaluated at the Gaussian quadrature points in all the elements comprising the cross-section. These stresses are evaluated through the constitutive law at the element level. In general, the rigid body displacements are known from the Saint–Venant solution. Based on end solutions with decay in both positive and negative z-direction, we can divide the end solution into two parts, i.e., from the tip end and the root end of the cantilevered beam of length L. To wit,

$$\begin{aligned}\mathbf{U}(z) &= \mathbf{U}_{\mathrm{SV}}(z) + \mathbf{\Phi}_{\mathbf{RB6}}(z)\mathbf{a}_{\mathbf{RB}} + \mathbf{\Phi}_{tip} diag(e^{-\gamma_j z})\mathbf{a}_{tip}\\ &\quad + \mathbf{\Phi}_{root} diag(e^{-\gamma_j (L-z)})\mathbf{a}_{root},\\ \mathbf{S}(z) &= \mathbf{S}_{\mathrm{SV}}(z) + \mathbf{S}_{tip} diag(e^{-\gamma_j z})\mathbf{a}_{tip} + \mathbf{S}_{root} diag(e^{-\gamma_j (L-z)})\mathbf{a}_{root}.\end{aligned} \tag{27}$$

In the most general case, effects at the root (tip) end will be felt at the tip (root) end, so that both parts of the end solution need to be considered. But for a sufficiently long beam, the effects on one end can be considered to be completely uncoupled from the other end. This can easily by assessed by examining the lowest eigenvalue, the effects of which persist the furthest into the interior. We will proceed under the assumption that the beam is sufficiently long, so that only one part of the end solution needs to be considered at the root and the tip ends.

Assuming that the boundary condition at the root–end, $z = L$, is full fixity, we have

$$\begin{aligned}\mathbf{U}(L) &= \mathbf{U}_{\mathrm{SV}}(z) + \mathbf{\Phi}_{\mathbf{RB6}}(z)\mathbf{a}_{\mathbf{RB}} + \mathbf{\Phi}_{root} diag(e^{-\gamma_j (L-z)})\mathbf{a}_{root}\big|_{z=L}\\ &= \mathbf{U}_{\mathrm{SV}}(L) + \mathbf{\Phi}_{\mathbf{RB6}}(L)\mathbf{a}_{\mathbf{RB}} + \mathbf{\Phi}_{root}\mathbf{a}_{root} \equiv \mathbf{0}\end{aligned} \tag{28}$$

as $diag(e^{-\gamma_j (L-z)}) = \mathbf{I}$ for $z = L$. Rearranging this equation gives

$$\underset{(3M\times n)}{\mathbf{\Phi}_{root}}\ \underset{(n\times 1)}{\mathbf{a}_{root}} = \mathbf{U}_L - \mathbf{U}_{\mathrm{SV}}(L) - \mathbf{\Phi}_{\mathbf{RB6}}(L)\mathbf{a}_{\mathbf{RB}}, \tag{29}$$

where $3M$ denotes the total number of kinematic degrees of freedom and n is the number of eigenmodes adopted for the analysis. Because not all of the eigenmodes are used (i.e., $3M \gg n$), algebraic system given in Eq. (29) is over-determined. The solution for the unknown amplitudes ($\mathbf{a}_{\mathbf{root}}$) can be sought by least squares, i.e.,

$$\mathbf{a}_{root} = [\mathbf{\Phi}_{root}^H \mathbf{\Phi}_{root}]^{-1} \mathbf{\Phi}_{root}^H [\mathbf{U}_L - \mathbf{U}_{\mathrm{SV}}(L) - \mathbf{\Phi}_{\mathbf{RB6}}(L)\mathbf{a}_{\mathbf{RB}}], \tag{30}$$

where $\mathbf{\Phi}_{root}^H$ is the Hermitian (i.e., conjugate transpose) of $\mathbf{\Phi}_{root}$.

We let the applied tractions be denoted by $\mathbf{S}$ at the tip end ($z = 0$). Supposing that this distribution, in general is not according to that of the Saint–Venant solution. Thus, we can represent the difference between $\mathbf{S}$ and that of the Saint–Venant solution – which is a self-equilibrated state – through the expression

$$\mathbf{S}(z) = \mathbf{S}_{\mathrm{SV}}(z) + \mathbf{S}_{tip} diag(e^{-\gamma_j z})\mathbf{a}_{tip}. \tag{31}$$

Using $\mathbf{S}_0$ denote the prescribed stress components at the Q Gaussian quadrature points of the total discretized model of the cross section, we have

$$\mathbf{S}_0^T = [\sigma_{xz1}, \sigma_{yz1}, \sigma_{zz1}, \ldots, \sigma_{xzQ}, \sigma_{yzQ}, \sigma_{zzQ}]\big|_{z=0}. \tag{32}$$

Similarly, extracting the same components from $\boldsymbol{\sigma}_{\mathrm{SV}}$ and $\boldsymbol{\sigma}_{tip}$, denoting them as $\mathbf{S}_{\mathrm{SV}}$ and $\mathbf{S}_{tip}$, and by invoking $diag(e^{-\gamma_j z}) = \mathbf{I}$ in Eq. (31), the traction boundary conditions can be written as

$$\mathbf{S}_0 = \mathbf{S}_{\mathrm{SV}}(0) + \mathbf{S}_{tip}\mathbf{a}_{tip} \rightarrow \underset{(3M\times n)}{\mathbf{S}_{tip}}\ \underset{(n\times 1)}{\mathbf{a}_{tip}} = \mathbf{S}_0 - \mathbf{S}_{\mathrm{SV}}(0). \tag{33}$$

Again, this algebraic system is over-determined as $3M \gg n$. The least-squares solution of Eq. (33) for $\mathbf{a}_{tip}$ yields

$$\mathbf{a}_{tip} = [\mathbf{S}_{tip}^H \mathbf{S}_{tip}]^{-1} \mathbf{S}_{tip}^H [\mathbf{S}_0 - \mathbf{S}_{SV}(0)], \tag{34}$$

where $\mathbf{S}_0$ denotes the prescribed traction conditions at the tip.

5.2. Analysis of transitional effects for connected cylinders

Here, we consider two dissimilar beams, A and B, as illustrated in Fig. 4 where beam B is fully bonded to A at interface Γ_1. We adopt the origins of the coordinate systems of the two beams as shown in this figure. In general, an axial load, bending moment and torque are applied at the free-end of beam B. Additionally, on the surface Γ_2 of beam A, there is the possibility of applied tractions $\mathbf{g}$ whose resultant may be an axial force, bending moment and torque. We wish to determine the complete displacement and stress fields in the vicinity of the interface of these the two beams. To simplify the analysis somewhat, we will assume both beams are sufficiently long, so that their conditions at the extreme ends are not coupled with those at the interface. Only functions with decay from the interface are considered. Then, the displacement fields for the two beams are

$$\begin{aligned} \mathbf{U}^A(z_1) &= \mathbf{U}_{SV}^A(z_1) + \mathbf{\Phi}_t^A \mathbf{a}^A + \mathbf{\Phi}_{RB}^A(z_1)\mathbf{a}_{RB}^A, \\ \mathbf{U}^B(z_2) &= \mathbf{U}_{SV}^B(z_2) + \mathbf{\Phi}_r^B \mathbf{a}^B + \mathbf{\Phi}_{RB}^B(z_2)\mathbf{a}_{RB}^B. \end{aligned} \tag{35}$$

The first step in the analysis is the determination of the Saint–Venant extension–bending-torsion solutions for each beam. In the Saint–Venant solution for beam A, global equilibrium must be observed to relate the resultant force and moments in member A to that of member B and the contributions of $\mathbf{g}$ on surface Γ_2. For beam A, it is also possible to determine the rigid body displacements from the conditions at $z_1 = L_A$. However, it is not possible to determine rigid body displacement $\mathbf{\Phi}_{RB}^B(z_2)\mathbf{a}_{RB}^B$ at this time.

Continuity conditions for the two beams involve displacements and stresses of the both beams at the interface. Expressions for displacement and stress fields in beam A at the interface are

$$\mathbf{U}^A|_{z_1=0} = \mathbf{U}_{SV}^A(0) + \mathbf{\Phi}_t^A \boldsymbol{\alpha}_t^A + \mathbf{\Phi}_{RB}^A \mathbf{a}_{RB}^A; \quad \mathbf{S}^A|_{z_1=0} = \mathbf{S}_{SV}^A(0) + \mathbf{S}(\mathbf{\Phi}_t^A)\boldsymbol{\alpha}_t^A \tag{36}$$

which can be organized further into terms on surfaces Γ_1 and Γ_2 as in

$$\begin{aligned} \begin{Bmatrix} \mathbf{U}_{\Gamma_1}^A \\ \mathbf{U}_{\Gamma_2}^A \end{Bmatrix} &= \begin{Bmatrix} \mathbf{U}_{SV_{\Gamma_1}}^A \\ \mathbf{U}_{SV_{\Gamma_2}}^A \end{Bmatrix} + \begin{bmatrix} \mathbf{\Phi}_{t1}^A \\ \mathbf{\Phi}_{t2}^A \end{bmatrix} \boldsymbol{\alpha}_t^A + \begin{bmatrix} \mathbf{\Phi}_{RB1}^A \\ \mathbf{\Phi}_{RB2}^A \end{bmatrix} \mathbf{a}_{RB}^A, \\ \begin{Bmatrix} \mathbf{S}_{\Gamma_1}^A \\ \mathbf{S}_{\Gamma_2}^A \end{Bmatrix} &= \begin{Bmatrix} \mathbf{S}_{SV_{\Gamma_1}}^A \\ \mathbf{S}_{SV_{\Gamma_2}}^A \end{Bmatrix} + \begin{bmatrix} \mathbf{S}_{t1}^A \\ \mathbf{S}_{t2}^A \end{bmatrix} \boldsymbol{\alpha}_t^A. \end{aligned} \tag{37}$$

These expressions in beam B at the interface, which occur only on Γ_1, are

$$\begin{aligned} \mathbf{U}^B|_{\Gamma_1} &= \mathbf{U}_{SV}^B(L_B) + \mathbf{\Phi}_r^B \boldsymbol{\alpha}_r^B + \mathbf{\Phi}_{RB}^B(L_B)\mathbf{a}_{RB}^B, \\ \mathbf{S}^B|_{\Gamma_1} &= \mathbf{S}_{SV}^B(L_B) + \mathbf{S}^B(\mathbf{\Phi}_r^B)\boldsymbol{\alpha}_r^B. \end{aligned} \tag{38}$$

To summarize, the unknowns in Eqs. (37) and (38) are coefficients $\boldsymbol{\alpha}_t^A$ and $\boldsymbol{\alpha}_r^B$ of the decay functions and amplitude $\mathbf{a}_{RB}^B$ of the rigid body displacement in beam B.

The interface (continuity) conditions are

$$\mathbf{U}^A|_{\Gamma_1} = \mathbf{U}^B|_{\Gamma_1}; \quad (\mathbf{S}^A + \mathbf{S}^B)|_{\Gamma_1} = 0; \quad \mathbf{S}^A|_{\Gamma_2} = \mathbf{g}. \tag{39}$$

Enforcing these conditions gives

$$\mathbf{U}_{SV_{\Gamma_1}}^A + \mathbf{\Phi}_{t1}^A \boldsymbol{\alpha}_t^A + \mathbf{\Phi}_{RB}^A \mathbf{a}_{RB}^A = \mathbf{U}_{SV}^B(L_B) + \mathbf{\Phi}_r^B \boldsymbol{\alpha}_r^B + \mathbf{\Phi}_{RB}^B(L_B)\mathbf{a}_{RB}^B, \tag{40}$$

$$\mathbf{S}_{SV_{\Gamma_1}}^A + \mathbf{S}_{t1}^A \boldsymbol{\alpha}_t^A + \mathbf{S}_{SV}^B(L_B) + \mathbf{S}_r^B \boldsymbol{\alpha}_r^B = 0, \tag{41}$$

$$\mathbf{S}_{SV_{\Gamma_2}}^A + \mathbf{S}_{t2}^A \boldsymbol{\alpha}_t^A = \mathbf{g}. \tag{42}$$

Recasting these equations in matrix form yields

$$\begin{bmatrix} \mathbf{\Phi}_{t1}^A & -\mathbf{\Phi}_r^B & -\mathbf{\Phi}_{RB}^B(L_B) \\ \mathbf{S}_{t1}^A & \mathbf{S}_r^B & 0 \\ \mathbf{S}_{t2}^A & 0 & 0 \end{bmatrix} \begin{Bmatrix} \boldsymbol{\alpha}_t^A \\ \boldsymbol{\alpha}_r^B \\ \mathbf{a}_{RB}^B \end{Bmatrix} = \begin{Bmatrix} \mathbf{U}_{SV}^B(L_B) - \mathbf{U}_{SV_{\Gamma_1}}^A - \mathbf{\Phi}_{RB}^A \mathbf{a}_{RB}^A \\ -\mathbf{S}_{SV}^B(L_B) - \mathbf{S}_{SV_{\Gamma_1}}^A \\ \mathbf{g} - \mathbf{S}_{SV_{\Gamma_2}}^A \end{Bmatrix} \tag{43}$$

or

$$\mathbf{A}\boldsymbol{\alpha} = \mathbf{b}. \tag{44}$$

This over-determined problem can be solved to obtain the unknown amplitudes $(\boldsymbol{\alpha})$ using a least–squares approach as in

$$\mathbf{A}^H \mathbf{A}\boldsymbol{\alpha} = \mathbf{A}^H \mathbf{b} \Rightarrow \boldsymbol{\alpha} = [\mathbf{A}^H \mathbf{A}]^{-1} \mathbf{A}^H \mathbf{b}. \tag{45}$$

6. Application problems

6.1. Interlaminar stresses decaying from the tip-end of a laminated beam

Here, we consider a square-shaped cantilevered sandwich beam, with isotropic top and bottom layers and an orthotropic core, as illustrated in Fig. 5. Material properties of the orthotropic core are typical of a graphite–epoxy composite, i.e.,

$$\frac{E_L}{E_T} = 10, \quad \frac{G_{LT}}{E_T} = 0.4, \quad \frac{G_{TT}}{E_T} = 0.3, \quad \nu_{LT} = 0.3, \quad \nu_{TT} = 0.25, \tag{46}$$

where subscripts L and T denote longitudinal and transverse directions, respectively. Young's modulus and Poisson's ratio for the isotropic layers are E and $\nu = 0.3$. In this example, we assume that $E = E_T$.

We consider three sets of applied tractions at the tip end of the beam whose resultants are an axial force, a bending moment, and a torque. The manner in which they are applied is shown in Fig. 5. We wish to determine how these applied tractions evolve into Saint–Venant distributions of extension, bending and torsion, or alternatively how the self-equilibrated fields attenuate into the interior of this beam. The relevant stress components at the point marked as A in Fig. 5 on the interface between the layers are monitored along the beam's axial direction.

Plots in Fig. 6 show the decay of various stress components along the longitudinal axis passing through the interface between the top layer and the core for three different orientations of the natural elastic axes of the orthotropic core with respect to the coordinate directions, viz., 0°, 45°, and 90°. Also in this figure, SAFE results are compared with three-dimensional finite element method results obtained using (ANSYS, 1998); and, again, there is a very good agreement between the two sets of results.

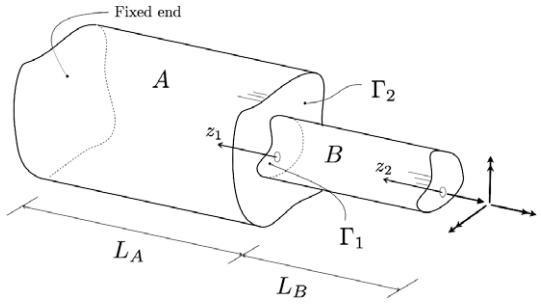

Fig. 4. The geometry of a generic end-to-end connected beam problem.

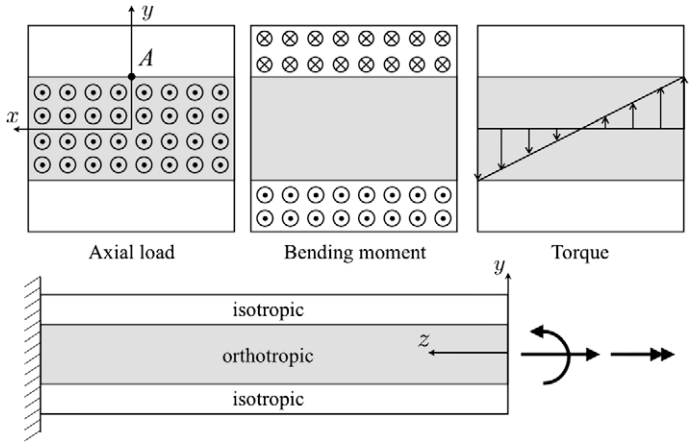

Fig. 5. The geometry and loading conditions of the sandwich beam validation problem. The top and bottom layers are made of the same isotropic material with an orthotropic core.

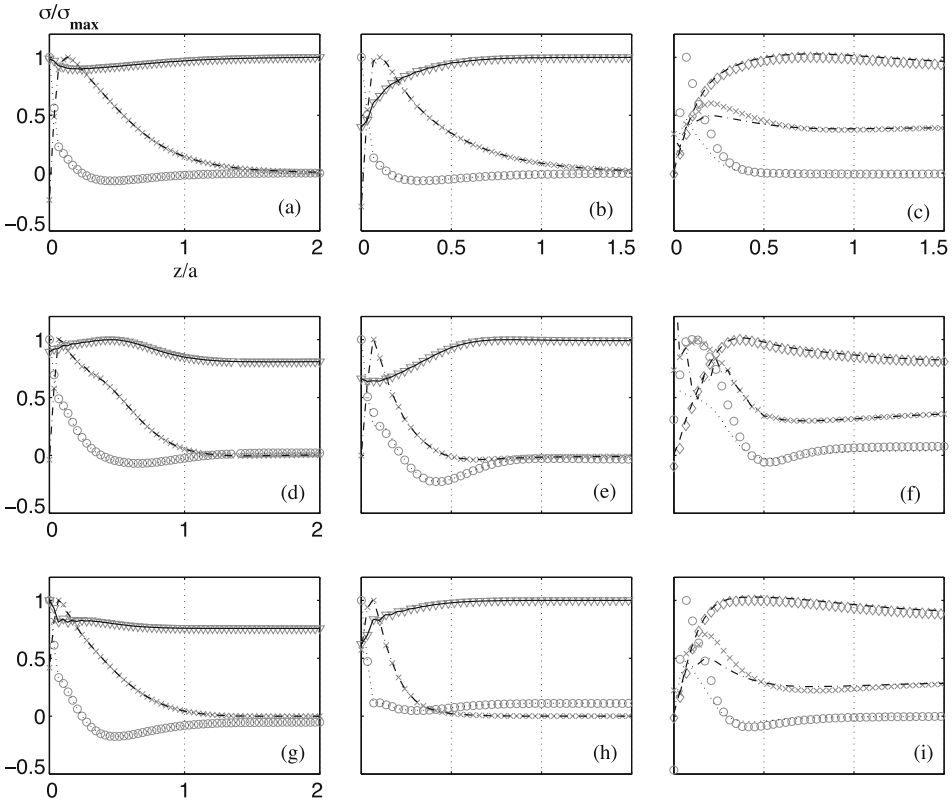

Fig. 6. Comparison of stresses decaying from the free end of a sandwich beam. Symbols ($\sigma_{zz}(\triangledown)$; $\sigma_{yy}(\bigcirc)$; $\sigma_{yz}(\times)$; $\sigma_{xz}(\diamondsuit)$) and the (dashed, dotted, etc.) lines denote the SAFE solutions and 3-D finite element solutions, respectively. The stress axis is normalized with respect to the maximum absolute value of the corresponding stress component. The longitudinal axis (along the axial dimension) is normalized with respect to the length of a side of the square cross-section. The columns starting with (a), (b), (c) are the cases of extension, bending and torsion, respectively. The rows starting with (a), (d), (g) are for the three different orientation of the orthotropic material at the core of the cross-section, namely 0°, 45°, 90°, respectively.

Comparisons were made with ANSYS because an analytical solution of this problem does not exist to the best of our knowledge.

Table 3 provides the normalized (with respect to the depth A of the cross-section) characteristic decay lengths of the relevant interlaminar stresses for the extension–bending–torsion problem for different orientations of the orthotropic core. Following Miller and Horgan (1995), we define the characteristic decay length L^* as the length over which the stresses decay to 1% of their values

Table 3
Normalized characteristic decay lengths of interlaminar stresses (given as percent of cross-sectional dimension) for different material orientations of the orthotropic core.

	Extension		Bending		Torsion	
	σ_{yy}	σ_{yz}	σ_{yy}	σ_{yz}	σ_{yy}	σ_{yz}
0°	5.17	67.2	5.17	48.3	20.7	48.3
45°	13.8	62.1	6.90	22.4	31.7	34.4
90°	6.90	51.7	4.60	20.7	19.5	34.4

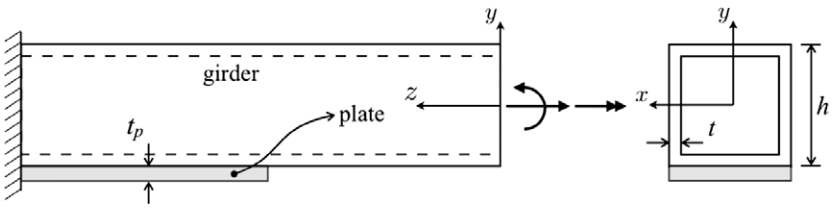

Fig. 7. The geometry and loading conditions of a girder retrofitted by a thin plate. The beam is cantilevered and loaded at the tip-end.

at $z = 0$. Thus, $L^* \equiv \ln 100/\lambda^*$, where λ^* is the real part of the lowest eigenvalue in Eq. (27) viz. Eq. (3).

We note here that the SAFE analysis is significantly less computationally intensive than the ANSYS analysis, as two-dimensional rather than three-dimensional finite element modeling is employed. From an examination of the eigendata, one can immediately estimate the 3D element length required in the axial distance in ANSYS to capture the behavior. It is easily seen that a relatively fine discretization is needed to determine the behavior of the decay accurately (to obtain the results shown a very fine graded 3D mesh containing approximately 1500 linear brick elements was used for ANSYS, whereas SAFE results were obtained using a 2D mesh comprising 81 quadrilateral elements). Moreover, once a set of two-dimensional eigendata is established, it is possible to use it for any distribution of end effects.

6.2. Transition effects in a plate-reinforced box girder

Here, we consider a hollow beam reinforced with a plate over a partial distance as illustrated in Fig. 7. We assume that the end of the plate is sufficiently remote from the end of the beam so that end effects there do not interfere with the analysis in the transition zone. Then, we can use the procedure set forth in Section 5.2.

We set the material properties for the hollow beam and plate as $E_b = 210$ GPa, $\nu_b = 0.3$, and $E_p = 300$ GPa, $\nu_p = 0.3$; and the dimensions shown in Fig. 7 as $h = 80$ cm, $t = 4$ cm, $t_p = 0.4$ cm. We consider all three loading cases (extension, bending, and torsion) and investigate the interlaminar (or delamination) stresses decaying along the length of the plate, and compare SAFE results with those determine through (ANSYS, 1998). We also note that the agreement between the SAFE and ANSYS results are again very good. But, as pointed out in the previous example, the SAFE method is far more efficient computationally than ANSYS. ANSYS results are merely included to show the validity of the SAFE approach in this example, where the cross-sectional geometry of the beam has a discontinuity.

The interlaminar stresses decaying from the interface are shown in Fig. 8 for the three loading cases considered. In this normalized stress plot, we can see that the decay lengths of the interfacial stresses are not highly sensitive to the loading type. We also observe that at a distance of around 0.15 h from the cross-sectional discontinuity, the interfacial normal stress decays to an insignificant level, but the interfacial shear stress σ_{yz} persists into the interior nearly four times that distance.

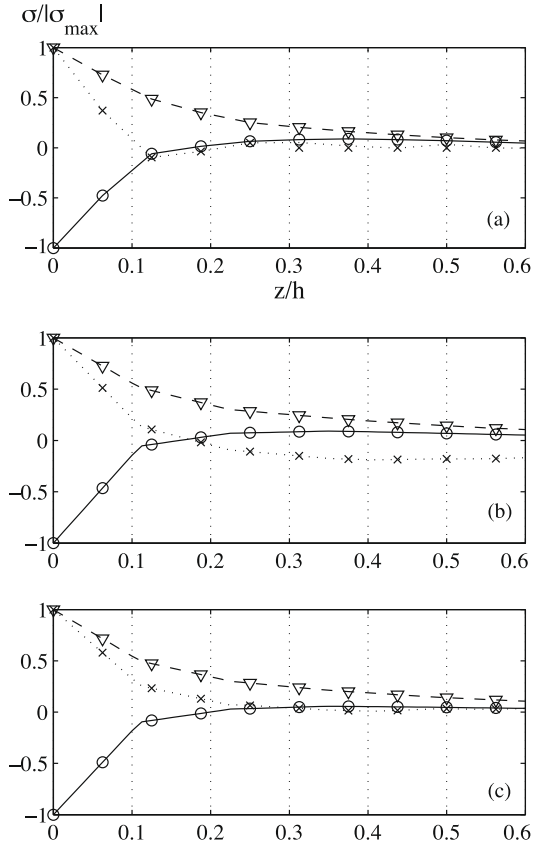

Fig. 8. Comparison of interlaminar stresses along the interface between the girder and the plate for (a) extension (b) bending, (c) torsion. The symbols (σ_{yy}(◯); σ_{xy} (×); σ_{yz} (▽)) and the (dashed, dotted, etc.) lines denote the SAFE and 3-D finite element solutions respectively.

6.3. Laminated beams: a parametric study on the effect of material properties

Another problem we examine with the SAFE method is the determination of interlaminar stresses near the tip-end of a composite beam under a tensile patch load (cf., Fig. 9). The beam is composed of two laminates, having the same material properties (transverse isotropy), but different fiber orientations. We use five different ply orientations in a parametric study – namely, $[0^\circ, \pm 30^\circ, \pm 45^\circ, \pm 60^\circ, \pm 90^\circ]$. Case 0° corresponds to a homogeneous, transversely isotropic beam with fibers oriented along the z–axis, and 90° corresponds to again a homogeneous transversely isotropic beam, however with fibers oriented along the x-axis.

Fig. 10 shows how the interlaminar (delamination) stresses (σ_{yy}, σ_{yz}, and σ_{xy}) for different fiber orientations change, as we move away from the free-end. We observe from the figure that it is not always the strongest orientation of the plies that causes the smallest interlaminar stresses. Some of the mechanical properties of a composite (e.g., its strength or weight) may be sacrificed in favor of decreasing the interlaminar stresses. As such, Fig. 10 may be used in order to achieve an optimum design of such a structure by obtaining the desired strength with limited interlaminar stresses. A failure criterion (for example von Mises) may also be employed with the aid of Fig. 10 to decide which orientation of the laminates is least susceptible to such a failure.

In our discussion of delamination, we need to distinguish between that from the lateral surface(s) of a beam and that from its end. Interlaminar stresses from a lateral surface (which may or may not be uniform over the length of the beam) require a rel-

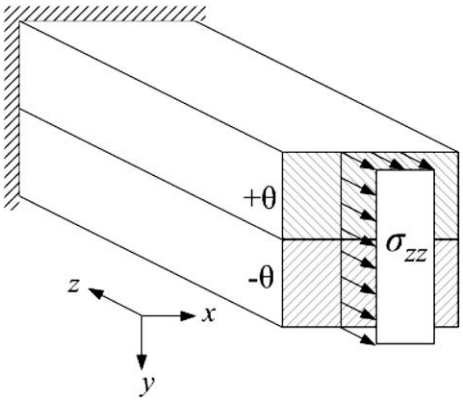

Fig. 9. Problem geometry: a two-layer laminated composite cantilever beam, under a symmetric patch load.

atively fine finite element discretization of the cross-section to properly define the decay phenomenon. This has been considered by many authors (e.g., Pipes and Pagano, 1970; El Fatmi and Zenzri, 2004), but is not within the scope of the present study.

6.4. End-to-end connected beams: a parametric study on the effects of the difference in material properties

The final problem we consider is a parametric study for investigating how the differences in material properties affect the stress transition in end-to-end connected beams. For this, we connect two isotropic beams as shown in Fig. 11, with Young's Moduli E_1 and E_2, and Poisson's ratios v_1 and v_2, and apply axial loading with resultant P. There are no transition effects when $E_1 = E_2$ and $v_1 = v_2$. However, stress concentrations and jumps in certain stress components near the transition zone are naturally expected, as the difference in material properties increases. We determine these stress concentrations with respect to two parameters, namely the ratio of the Young's Moduli E_1/E_2, and of the Poisson's ratios v_1/v_2 for the two beams.

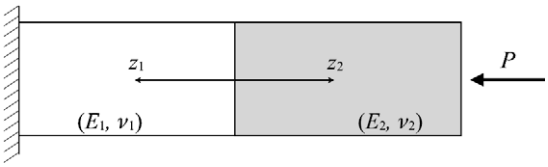

Fig. 11. Two rectangular isotropic beams, connected end-to-end, with different Young's Moduli E and Poisson's ratios v.

Fig. 12 shows how the difference between the maximum value of the stress component in the transition zone, σ_{max}, and the far field values (i.e., the Saint–Venant solution) σ_{sv} of that stress component, changes as the parameters are altered. For the stress components plotted in Fig. 11, the Saint–Venant stresses are: $\sigma_{xx-sv} = \sigma_{yy-sv} = \sigma_{yz-sv} = 0$, and $\sigma_{zz-sv} = 1.0$. It can be seen that the stress components σ_{xx} and σ_{yz} reach significant values in the transition zones, as the properties of the two materials become further apart. The axial stress (σ_{zz}), which is the most significant stress component for the extension problem, reaches values as high as 5 times the far-field magnitude.

7. Conclusions

In this study, we extensively verified a semi-analytical finite element (SAFE) method – put forth earlier by Dong and co-workers (cf., Dong et al., 2001; Kosmatka et al., 2001; Lin et al., 2001) – for analysis of end-effects in inhomogeneous, anisotropic cylinders. In the SAFE approach an algebraic eigenvalue problem is introduced using the semi-analytical governing equations. Then the solution field is expressed through an expansion of decaying eigen-modes. Our verification studies involving comparisons to both analytical and fully-discrete methods have shown that the SAFE approach is highly accurate – even when relatively simple/coarse meshes are used to discretized the cross-sectional geometry.

We further extended/generalized the SAFE method to handle transitional effects in connected beams where discontinues in cross-sectional geometry and/or material constitution occur. Using a similar eigenvalue expansion, we enforced the continuity of dis-

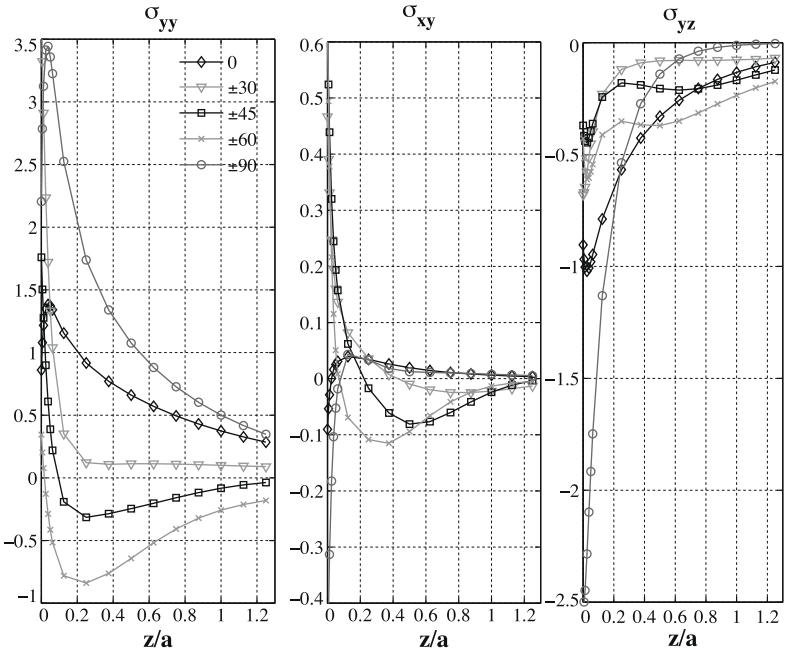

Fig. 10. Interlaminar stresses for a two-layer laminated beam under extension, for different fiber orientation of the transversely isotropic layers.

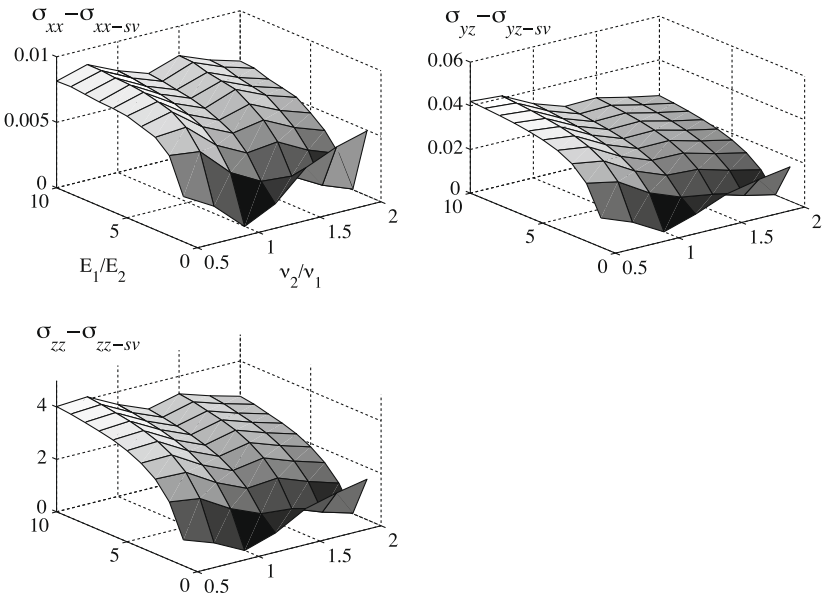

Fig. 12. Parametric plots showing the influence of difference in material properties of two beams on the transition effects. The E_1/E_2 and ν_1/ν_2 axes respectively denote the ratios of Young's Moduli and Poisson's ratios of the two isotropic beams, connected as shown in Fig. 11. The elevation axis is the difference between the maximum value of the stress component near the transition zone and the Saint–Venant value (far-field) of that stress component, i.e. $\sigma_{max}-\sigma_{sv}$.

placement and stress fields in a least-squares sense. We examined transitional effects and stress concentrations for a plate reinforced beam to verify the formulation and to assess its performance compared to the conventional three-dimensional finite element method.

Finally, we conducted parametric studies in two simple problems with implications to engineering practice to demonstrate the potential utility of the proposed method. Such parametric studies are prohibitive through three-dimensional finite element analyses. Our experience in these problems indicated that the SAFE method is extremely efficient compared to 3D FEM. It appears possible to utilize the method as the analysis engine in optimization problems involving the design of composite beams and their transition zones whereby cross-sectional shapes, material layering, and material properties are parametrically manipulated for improved performance and function.

Acknowledgements

The research reported herein was supported by the National Science Foundation under Grant No. CMS-0547670, and in part, by funding from the Faculty Grants Program of UCLA Academic Senate Council on Research. This support is gratefully acknowledged. The opinions expressed in this paper are those of the authors and do not necessarily reflect those of the sponsors.

References

ANSYS, September 1998. Coupled-Field Analysis Guide. ANSYS Release 5.5, 3rd ed.
de Saint-Venant, A.J.C.B., 1855. Memoire sur la torsion des prismes. Mém. Savants Étrangers, Acad. Sci. Paris 14, 223–560.
de Saint-Venant, A.J.C.B., 1856. Memoire sur la flexion des prismes. J. Math. Liouville 1, 89–189.
Dong, S.B., Huang, K.H., 1985. Edge vibrations in laminated composite plates. J. Appl. Mech., ASME 52 (2), 433–438.
Dong, S.B., Kosmatka, J.B., Lin, H.C., 2001. On Saint-Venant's problem for an inhomogeneous, anisotropic cylinder. Part I. Saint-Venant solutions. ASME, J. Appl. Mech. 68 (3), 376–381.
El Fatmi, R., 2007a. Non-uniform warping including the effects of torsion and shear forces. Part I: a general beam theory. Int. J. Solids Struct. 44, 5912–5929.
El Fatmi, R., 2007b. Non-uniform warping including the effects of torsion and shear forces. Part II: analytical and numerical applications. Int. J. Solids Struct. 44, 5930–5952.
El Fatmi, R., Zenzri, H., 2002. On the structural behavior and the Saint-Venant solution in the exact beam theory. Application to laminated composite beams. Comput. Struct. 80, 1441–1456.
El Fatmi, R., Zenzri, H., 2004. A numerical method for the exact beam theory. Application to homogeneous and laminated beams. Int. J. Solids Struct. 41, 2521–2537.
Giavotto, V., Borri, M., Mantegazza, P., Ghiringhelli, G., Carmaschi, V., Maffioli, G.C., Mussi, F., 1983. Anisotropic beam theory and applications. Comput. Struct. 16, 403–413.
Goetschel, D.B., Hu, T.B., 1985. Quantification of Saint–Venant's principle for a general prismatic member. Comput. Struct. 21, 869–874.
Herrmann, L.R., 1965. Elastic torsional analysis of irregular shapes. J. Engr. Mech. Div., ASCE 91 (EM6), 11–19.
Horgan, C.O., 1989. Recent developments concerning Saint-Venant's principle: an update. Arch. Rat'l Mech. Anal., 295–303.
Horgan, C.O., Knowles, J.K., 1983. Recent developments concerning Saint-Venant principle. Adv. Appl. Mech. 23, 179–269.
Huang, K.H., Dong, S.B., 1984. Propagating waves and standing vibrations in a composite cylinder. J. Sound Vibr. 96, 363–379.
Ieşan, D., 1986. On Saint–Venant's problem. Arch. Rat. Mech. Anal. 91, 363–373.
Johnson, M.W., Little, R.W., 1965. The semi-infinite strip. Quart. Appl. Math. 22, 335–344.
Kazic, M., Dong, S.B., 1990. Analysis of restrained torsion. J. Eng. Mech. Div. 116, 870–891.
Knowles, J.K., 1966. On Saint–Venant's principle in the two-dimensional linear theory of elasticity. Arch. Rat. Mech. Anal. 22, 1–22.
Kosmatka, J.B., Lin, H.C., Dong, S.B., 2001. On Saint-Venant's Problem for an inhomogeneous, anisotropic cylinder. Part II: cross-sectional properties. ASME J. Appl. Mech. 68 (3), 382–391.
Ladevéze, P., Simmonds, J., 1998. New concepts for linear beam theory with arbitrary geometry and loading. Eur. J. Mech., A/Solids 17, 377–402.
Lin, H.C., Dong, S.B., 2006. On the Almansi–Michell problems for an inhomogeneous, anisotropic cylinder. J. Mech. 22 (1), 51–57.
Lin, H.C., Dong, S.B., Kosmatka, J.B., 2001. On Saint-Venant's problem for an inhomogeneous, anisotropic cylinder. Part III. End effects. ASME, J. Appl. Mech. 68 (3), 392–398.
Little, R.W., Childs, S.B., 1967. Elastostatic boundary region problem in solid cylinders. Quart. Appl. Math. 25, 261–274.
Mason, W.E., Herrmann, L.R., 1968. Elastic shear analysis of general prismatic beams. J. Eng. Mech. Div., ASCE, 94.
Miller, K.L., Horgan, C.O., 1995. Saint–Venant end effects for plane deformations of elastic composites. Mech. Compos. Mater. Struct. 2, 203–214.
Pipes, R.B., Pagano, N.J., 1970. Interlaminar stresses in composite laminates under uniform axial extension. J. Compos. Mater. 4, 538–548.
Popescu, B., Hodges, D.H., 2000. On asymptotically correct Timoshenko-like anisotropic beam theory. Int. J. Solids Struct. 37, 535–558.
Synge, J.L., 1945. The problem of Saint Venant for a cylinder with free sides. Quart. Appl. Math. 2, 307–317.
Taweel, H., Dong, S.B., Kazic, M., 2000. Wave reflection from the free end of a cylinder with an arbitrary cross-section. Int. J. Solids Struct. 37, 1701–1726.
Toupin, R.A., 1965. Saint–Venant's principle. Arch Rat. Mech. Anal. 18, 83–96.